



United States Department of Commerce
Technology Administration
National Institute of Standards and Technology

NIST Technical Note 1392

**Time-Domain Calibrations
of D-Dot Sensors**

Robert T. Johnk
Arthur R. Ondrejka

NIST Technical Note 1392

Time-Domain Calibrations of D-Dot Sensors

Robert T. Johnk
Arthur R. Ondrejka

Electromagnetic Fields Division
Electronics and Electrical Engineering Laboratory
National Institute of Standards and Technology
325 Broadway
Boulder, Colorado 80303-3328

February 1998



U.S. DEPARTMENT OF COMMERCE, William M. Daley, Secretary
TECHNOLOGY ADMINISTRATION, Gary R. Bachula, Acting Under Secretary for Technology
NATIONAL INSTITUTE OF STANDARDS AND TECHNOLOGY, Raymond G. Kammer, Director

National Institute of Standards and Technology Technical Note
Natl. Inst. Stand. Technol., Tech. Note 1392, 36 pages (February 1998)
CODEN:NTNOEF

U.S. GOVERNMENT PRINTING OFFICE
WASHINGTON: 1998

For sale by the Superintendent of Documents, U.S. Government Printing Office, Washington, DC 20402-9325

CONTENTS

	<u>Page</u>
1. INTRODUCTION.....	1
2. D-DOT SENSOR DESCRIPTIONS	2
3. SENSOR CALIBRATION PROCEDURES IN THE TEM CELL	2
4. SENSOR CALIBRATIONS ON THE CONE AND GROUND PLANE.....	4
5. NOISE REDUCTION	6
6. TRANSFER FUNCTION RESULTS	7
7. UNCERTAINTIES IN THE MEASUREMENT SYSTEMS	9
8. CONCLUSIONS	12
9. REFERENCES.....	12

LIST OF TABLES

Table 1. Type B expanded uncertainties (from Ref. [9]) for sensor calibrations in the NIST 1.2 m TEM cell field generation system with an assumed confidence level of 95%.	9
Table 2. Type B expanded uncertainties (from Ref. [9]) for sensor calibrations in the NIST 1.2 m cone and ground plane cell field generation system with an assumed confidence level of 95%.	10
Table 3. Type A relative uncertainties computed from the Student's t-distribution [10,11] for a 95% level of confidence.	11
Table 4. NASA D-dot sensor average receive transfer function results, along with associated combined standard uncertainties (95% level of confidence). Note: bp denotes the support structure of sensor #34.	12

LIST OF FIGURES

Figure 1. Basic features of the D-Dot sensor used in the NASA evaluation effort.	14
Figure 2. Support structures for sensors #33, #34, #35, and #37. Sensor #36 had no supporting structure other than the small base plate shown in Figure 1.	15
Figure 3. TEM cell sensor calibration setup.	16
Figure 4. Low-frequency pulse generator output used for the TEM cell sensor calibrations.	16
Figure 5. Reference waveform acquisition setup for both TEM cell and cone and ground plane sensor calibrations.	17
Figure 6. Sensor #36 output waveform obtained with the TEM cell standard field generation system using the generator waveform of Figure 4.	17
Figure 7. Cone and ground plane sensor calibration setup.	18
Figure 8. High-frequency pulse generator output used for the cone and ground plane sensor calibrations.	19
Figure 9. Sensor #36 output waveform obtained with the cone and ground plane standard field generation system using the generator waveform of Figure 8.	19

Figure 10. Pre-trigger common-mode signal removal using SMA coaxial barrel without a center conductor.	20
Figure 11. Raw sensor #37 output obtained with the cone and ground plane system without averaging or common-mode signal removal.	21
Figure 12. Raw sensor #37 output obtained with the cone and ground plane system with 1024 averages. Note the significant reduction in high-frequency random variations.	21
Figure 13. Pre-trigger common mode signal detected by sensor #37. 1024 averages.	22
Figure 14. Sensor #37 output after 1024 averages and pre-trigger common-mode signal removal. The sensor response occurs approximately in the range of 3 ns to 9 ns, and the environmental reflections begin at approximately at 11 ns.	22
Figure 15. Sensor #36 receiving transfer function results obtained with the TEM cell standard field generation system.	23
Figure 16. Sensor #36 receiving transfer function results obtained with the cone and ground plane standard field generation system.	23
Figure 17. Intercomparison of sensor #36 receiving transfer function results obtained with the TEM cell and cone and ground plane standard-field generation systems.	24
Figure 18. Sensor #37 receiving transfer function results obtained with the TEM cell standard field generation system.	24
Figure 19. Sensor #37 receiving transfer function results obtained with the cone and ground plane standard field generation system.	25
Figure 20. Intercomparison of sensor #37 receiving transfer function results obtained with the TEM cell and cone and ground plane standard-field generation systems.	25
Figure 21. Sensor #33 receiving transfer function results obtained with the TEM cell standard field generation system. These data were obtained with the cylindrical post behind the sensor (with respect to the incident wavefront).	26
Figure 22. Sensor #33 receiving transfer function results obtained with the cone and ground plane standard field generation system. These data were obtained with the cylindrical post behind the sensor (with respect to the incident wavefront).	26
Figure 23. Sensor #33 receiving transfer function results obtained with the cone and ground plane standard field generation system. These data were obtained with the cylindrical post in front of the sensor (with respect to the incident wavefront).	27

Figure 24. Intercomparison of sensor #33 receive transfer function results obtained with the TEM cell and cone and ground plane standard-field generation systems. These data were obtained with the cylindrical post behind the sensor (with respect to the incident wavefront).....	27
Figure 25. Sensor #34 receiving transfer function results obtained with the TEM cell standard field generation system. These data were obtained with the narrow baseplate dimension parallel to the incident wavefront.	28
Figure 26. Sensor #34 receiving transfer function results obtained with the cone and ground plane standard field generation system. These data were obtained with the narrow baseplate dimension parallel to the incident wavefront.	28
Figure 27. Sensor #34 receiving transfer function results obtained with the cone and ground plane standard field generation system. These data were obtained with the wide baseplate dimension parallel to the incident wavefront.	29
Figure 28. Intercomparison of sensor #34 receiving transfer function results obtained with the TEM cell and cone and ground plane standard-field generation systems. These data were obtained with the narrow baseplate dimension parallel to the incident wavefront.....	29
Figure 29. Ungated sensor #35 time-domain response obtained on the cone and ground plane standard-field generation system. Note that the sensor response is extended by resonances in the support structure.....	30
Figure 30. Sensor #35 receiving transfer function results obtained with the cone and ground plane standard field generation system.....	30

TIME-DOMAIN CALIBRATIONS OF D-DOT SENSORS

Robert T. Johnk and Arthur R. Ondrejka

Electromagnetic Fields Division
National Institute of Standards and Technology
Boulder, Colorado 80303

This technical note covers in detail the procedures that are necessary to measure the receiving transfer function of broadband electric-field sensors using direct-pulse, time-domain methods. The calibration techniques presented here are applied to a cone and ground plane system in the 50 MHz to 14 GHz frequency range, as well as to a TEM cell in the 10 MHz to 100 MHz range. Measurement results using both types of facilities are presented for selected D-Dot sensors. In addition to a comparison of results from the two measurement facilities in the overlapping frequency range, a thorough combined uncertainty analysis is presented.

Key words: averaging; antenna; cone; common-mode; d-dot; electric-field; ground plane; oscilloscope; pulse generator; TEM cell; uncertainty.

1. INTRODUCTION

The National Aeronautics and Space Administration (NASA) recently conducted field tests on large commercial aircraft. The aircraft was flown close to various high-power electromagnetic radiators (air surveillance radars, broadcast transmitters, etc.) in order to measure the resulting fields at key locations of the airframe. The goal of this effort is to assess the impact of electromagnetic radiation on aircraft avionics systems and potential electromagnetic interference aircraft safety hazards.

In order to perform this study, NASA placed electromagnetic sensors at strategic internal and external locations on the aircraft, such as the passenger compartment, cargo bay, and key avionics bays. NASA chose linear electric-field sensors known as D-Dot sensors which, at sufficiently low frequencies, produce output voltages that are proportional to the time derivative of an impinging electric field [1]. At higher frequencies, for which the sensor critical dimensions become comparable to the wavelength of the incident field, this derivative property is lost as the sensor enters the resonance region and operates in a manner similar to a monopole antenna. The sensor outputs were fed into calibrated spectrum analyzers that recorded the results at selected frequencies in the 25 MHz to 6 GHz band. In order to determine the electric fields that were present, the sensors must be calibrated with incident fields that have known spatial and temporal properties, from which the mathematical relationships between the incident field and the output

voltage can be extracted. A sensor calibration over a wide frequency range is a requirement in order to obtain meaningful electric field measurement results.

The National Institute of Standards and Technology (NIST) in Boulder, Colorado has several facilities that enable the accurate and efficient calibration of electromagnetic sensors over such a wide frequency range. Two facilities that were used to generate a standard reference fields for the calibration of the NASA sensors were the TEM cell and the cone and ground plane system. The TEM cell is a closed transmission line system that generates reference fields from DC to a frequency at which the first higher-order modes occur, depending on the dimensions of the cell. For the 1.2 m TEM cell that was used in this effort, this frequency range is 0 to 100 MHz. The cone and ground plane system is used to extract the sensor receive transfer function in the range of 50 MHz to 14 GHz. The cone and ground plane is an open 200 Ω (nominal) transmission line system that generates an incident field with a simple mathematical representation that depends solely on geometry, making it a highly accurate primary standard. The only drawback of this system is the time window limitation of 11 ns dictated by the length of the cone and area of the ground plane. However, since the response times of a wide variety of electromagnetic sensors are less than 11 ns, this facility is highly useful for calibrations.

2. D-DOT SENSOR DESCRIPTIONS

Five different sensor configurations were calibrated in this effort. A sketch of the sensor that was tested is provided in Fig. 1. As the sketch shows, the sensor has a simple geometrical and mechanical structure consisting of mounting plate, a coaxial connector, and a solid metal central element. Structural support is provided by a plastic cylindrical shell. The sensor is designed to be used on a large, highly conducting ground plane, with the connecting cable and associated instrumentation located on the opposite side of the ground plane from the sensor element.

The sensors were deployed in five different configurations ranging from an actual ground plane mount to four different combinations of sensor and metal plate support structures. Sketches of the four sensor / metal plate structure configurations are depicted in Fig. 2. The first sensor (Serial #36) had no associated structure, and it was deployed by bolting it directly to the ground plane, in accordance with the manufacturer's specifications. The second sensor (Serial #37) had an attached sheet-metal base plate. The third sensor (Serial #33) had a slightly more complex structure associated with it, consisting of a metal base plate with a cylindrical post (used for mounting purposes). The fourth sensor configuration (Serial #34) was mounted an angled piece of sheet metal, with two of the sides left open to the environment. This sensor was elevated approximately 0.1 m above the ground plane. The fifth and final sensor (Sensor #35) was mounted centrally on the top of a 0.77 m high metal box. NASA requested that four of the sensors be calibrated on these structures to see how performance would be affected.

3. SENSOR CALIBRATION PROCEDURES IN THE TEM CELL

The TEM cell sensor calibration setup is depicted in Fig. 3. The TEM cell is a 50 Ω , matched stripline transmission structure that generates electric and magnetic fields that can readily be predicted from a known applied voltage [2]. The sensor under test is placed on the floor of the

cell along the longitudinal axis at the midpoint of the cell. This location is one of good field uniformity, and it is convenient for connecting cables without inducing severe common-mode signals. The cell is terminated with a precision broadband 50 Ω load, and is driven with a low-frequency, low-voltage pulse generator with a spectrum to 200 MHz. The pulse generator produces a unipolar waveform approximately 15 ns in duration at a repetition rate of 50 kHz. The generator output waveform across a matched 50 Ω load is depicted in Fig. 4.

In order to extract the required sensor parameters, two waveforms are needed: a reference signal from the generator itself and one from the output of the D-Dot sensor. The method by which the generator output reference waveform is obtained is shown in Fig. 5, where the output of the pulse generator is fed into the input of 20 GHz digitizing sampling oscilloscope, through a precision attenuator. The attenuator must be included to prevent severe nonlinear distortion or physical damage to the sampling head. The precision attenuator used in these measurements has a very flat insertion loss characteristic (less than 0.2 dB variation) and a very linear insertion phase over the frequency range of interest (10 MHz to 6 GHz), with resulting minimal dispersion. The second required waveform is the sensor output which is obtained by a direct connection to the sampling oscilloscope. In each case, the oscilloscope captures and digitizes both waveforms for subsequent signal processing on a computer.

A typical output waveform (sensor #36) obtained in the TEM cell depicted in Fig. 6. The initial portion of the waveform is due to the differentiating property of the sensor on the incident unipolar E-field pulse; the slight distortion that is visible on the initial doublet, along with the subsequent oscillations, are due to the occurrence of higher-order modes in the TEM cell. Previous studies [2], as well as the data obtained in this effort, indicate that the first non-TEM mode occurs around 130 MHz. This limits the upper usable frequency limit (for purpose of standard-field calibrations) of the cell to approximately 100 MHz.

The receiving transfer function [3,4] of the sensor is a frequency-domain quantity (with an assumed 50 Ω load) that requires a Fourier transformation process for both the reference and sensor time domain waveforms. The complete process of measuring the receive transfer function involves the following steps:

1. Using the ungated sensor output time domain waveform, compute the frequency domain spectrum amplitude [5] from 10 MHz to 100 MHz using a Fourier transformation. This can be effected using an FFT, chirp z-transform, or a series approximation to the Fourier integral. We used the series approximation because of simplicity and the ability to specify arbitrary frequency steps [6]. For the TEM cell, time gating is not required to eliminate the effects of higher-order modes since the filtering action of the Fourier transform algorithm provides the required suppression of higher-order mode effects and provides the required separation of sensor effects.
2. Compute the reference waveform amplitude spectrum using the ungated reference waveform using the same procedure as step 1. The reference waveform is obtained by feeding the pulse generator output through a precision 30 dB coaxial attenuator using the setup depicted in Fig. 5.
3. Take the ratio of the amplitude spectrum of step 1 to that of step 2. This division of spectral amplitudes in the frequency domain is referred to as deconvolution [7].

4. The required receive transfer function magnitude is finally obtained by multiplying the ratio obtained in step 3 by the TEM cell field geometry factors given in [2]. These geometry factors are a function of the cell dimensions as well as the location of the sensor under test.

This process is summarized in the following equations:

$$|TF_R(f)| = |K_{geom}| \left(\frac{|V_{sensor}(f)|}{|V_{in}(f)|} \right), \quad (1)$$

$$K_{geom} = \frac{V_{in}(f)}{E_{incident}(f)}.$$

In eq (1), f is the frequency of operation, $TF_R(f)$ is the receive transfer function; $V_{in}(f)$, $V_{sensor}(f)$ are the frequency-domain reference and sensor voltages; $E_{incident}(f)$ is the standard electric field illuminating the sensor. The applied voltage and the incident field are interrelated by the frequency-independent K_{geom} term that is a function of only the TEM cell geometry (provided that higher-order modes have been properly filtered out in the Fourier transformation process). This constant is governed by the quasi-static electric field configuration within the cell. This constant can be readily determined from tables and is provided in [2]. A method of moments code has also been developed at NIST that solves an electrostatic integral equation and generates an electric-field flux map of the of the cell [8]. Equation (1) assumes that this system, consisting of the TEM cell, pulse generator, oscilloscope, cables, and load, has 50Ω impedances throughout. Any variations from this value, due to mismatches in the scope, load, cables and cell, along with deviations from 50Ω of cell and cable characteristic impedances generate systematic errors in the predictions of eq (1). These mismatch errors are accounted for by increasing the estimated Type B uncertainties [6,9]. This issue is dealt with in a later section of this report.

4. SENSOR CALIBRATIONS ON THE CONE AND GROUND PLANE

For the frequency range of 50 MHz to 14 GHz, the cone and ground plane system, depicted in Fig. 7, is used. This system uses a 200Ω conical transmission line to generate an axially symmetric TEM spherical wave. The electric field generated by this system has the simple time-domain analytic form [3]:

$$E_{\theta}(t) = \frac{V_{base}(t - r/c)}{r \sin(\theta) \ln[\cot(\theta_0/2)]}, \quad (2)$$

where r , θ denote the location of the sensor under test, θ_0 is the solid angle of the cone (4° for the NIST system), and V_{base} is the total time domain voltage at the base of the cone given by

$$V_{base}(t) = V_{gen}(t)(1 + \Gamma), \quad (3)$$

with

$$\Gamma = \frac{Z_{cone} - Z_{gen}}{Z_{cone} + Z_{gen}}$$

subject to the time constraint:

$$0 \leq t < 11 \text{ ns}.$$

The elements in the numerator and denominator of the right side of eq (4) are the characteristic impedances of the pulse generator and cone, which, for the NIST system, are nominally 50 Ω and 200 Ω , respectively. Equations (2) and (3) are valid with the assumption of a purely forward-traveling wave that originates from the base of the cone. As soon as reflections occur, the equations are no longer valid, and the model becomes far more complicated. The dimensions of the cone and ground plane on the NIST system constrain the maximum usable time window to a maximum of 11 ns [3], which is quite satisfactory for the D-Dot sensors that were tested, as well as for a wide variety of other types of broadband sensors and antennas.

Sample reference and sensor waveforms for sensor #36 are shown in Figs. 8 and 9. The pulse produced by this generator is considerably faster than the one used for the TEM cell calibrations, and it has a usable spectrum (when received by these D-Dot sensors) up to 10 GHz. The sensor waveform has two principal contributions, the sensor response itself (3 ns < t < 6 ns) and the major reflections from the end of the cone, edges of the ground plane, and the walls, floor, and ceiling of the room (t > 13 ns). The sensor response portion of the waveform of Fig. 9 possesses a more complicated form than that obtained in the TEM cell, because this much faster pulse (with its much higher frequency content) excites a higher number of “antenna-like” modes on the sensor. The bipolar nature of the sensor response pulse is still indicative of low-frequency differentiating properties of the sensor.

The procedures used to calibrate the D-Dot sensor on the cone and ground plane are similar to those used in the TEM cell. As is shown in Fig. 7, the sensor is mounted on the ground plane at a suitable distance from the base of the cone that is within its projected volume. For the NASA calibrations the distance is set at $r = 2.3\text{m}$ and $\theta = 90^\circ$ to obtain the maximum usable time window. The base of the cone is driven by an impulse generator that produces a 10 V, 65 ps waveform, at a repetition rate of 50 kHz. The generator triggers a 20 GHz sampling oscilloscope that records the output of the sensor under test.

The calibration procedure involves the following steps:

1. Capture and time gate the sensor waveform. The objective of the time gating procedure is to delete undesired portions of the received waveforms by simply “zeroing” them out. In the case of the sensor waveform, the gating process completely eliminates the spurious reflections from the end of the cone, the edges of the ground plane, and the walls of the room.
2. Fourier transform the sensor waveform obtained in step 1, along with the reference waveform in a manner identical to that of the TEM cell.
3. Perform the required deconvolution procedure by computing the ratio of the sensor amplitude spectrum to the ratio of that of the reference sensor.
4. Multiply the result of step 3 by the analytical ratio of the frequency-domain input drive voltage to incident electric field to obtain the desired sensor receive transfer function magnitude.

This process is summarized as follows:

$$|TF_R(f)| = 0.625 |K_{cgp}| \left(\frac{|V_{sensor}(f)|}{|V_{gen}(f)|} \right), \quad (4)$$

with

$$K_{cgp} = 3.35 r \sin \theta.$$

In eq (4), K_{cgp} is the ratio of the voltage at the base of the cone to the generated electric field for the NIST system. This ratio depends solely on the location (r, θ) of the sensor under test. Since the voltage at the base of the cone and the resulting electric field have the same functional dependence in the time-domain, the Fourier-transformed ratio K_{cgp} of these quantities is independent of frequency for the fundamental, axially symmetric mode. Once again, only frequency-domain magnitudes are used in this case since phase information was not a requirement.

5. NOISE REDUCTION

Two significant interfering signal components were encountered during the sensor calibration process: random noise and common-mode noise. The random noise component was significant, due primarily to the ultrawide (20 GHz) bandwidth of the sampling oscilloscope. This component of noise is amenable to reduction by averaging over an ensemble of received waveforms [3]. The sampling oscilloscope that was used for this effort has a waveform built in averaging feature, and all of the captured waveforms were averaged 1024 times. The net effect of this process is a 30 dB reduction of random noise. The other interfering component, which is particularly severe in the cone and ground plane measurements, is due to common-mode signals that are generated by the test setup. Recent investigations at NIST have traced the source of this common-mode component to radiation from the rear panel of the pulse generator. This radiation generates a pre-trigger common mode signal that is synchronized with the trigger signal, and contaminates the entire received waveform with a deterministic error component. This effect is particularly severe with the cone and ground plane calibrations, due to the open system architecture. Although a common-mode signal was present in the TEM cell calibrations, the observed level was far smaller than that of the cone and ground plane. Observations of this signal component indicate that it is completely deterministic, so waveform averaging has no effect in reducing it. The impact of the common mode signal is twofold: it makes gating the received time signals ambiguous since there are no obvious points at which to set the gate, and it causes systematic errors in the frequency-domain receive transfer function measurements.

In order to reduce greatly the common-mode component, the following three-step subtraction procedure was found to be very effective:

1. The averaged sensor waveform with the common-mode signal component is acquired and stored.
2. A coaxial barrel is inserted in series with the generator feed line at the coaxial connector at the base of the cone. The sensor waveform is then averaged, captured, and stored. This barrel,

depicted in Fig. 10, has its inner conductor removed, providing isolation from the pulse generator and still permitting the common-mode currents to flow on the outer conductor of the generator, trigger, and sensor coaxial cables. The net result of this measurement is a deterministic common-mode signal.

3. Subtract the waveform obtained in step 2 from that of step 1. The result is a signal with at least a 40 dB reduction in common mode.

The effects of signal averaging and common-mode subtraction are illustrated in Figs. 11 through 14. Figure 11 depicts a single time-domain waveform captured by the sampling oscilloscope using sensor #37 on the NIST cone and ground plane system. The waveform is heavily contaminated with high-frequency random noise. A deterministic common mode signal is also readily visible. The result of applying 1024 waveform averages is shown in Fig. 12, where the random noise component is significantly reduced, but the common mode component remains. The common-mode waveform is shown in Fig. 13. This component is clearly visible on portions of the waveform of Fig. 12, where the sensor response and reflections are not present. The subtraction of the common-mode signal from that of Fig. 12 results in the clean and easily gated result in Fig. 14. Once the previously described three-step process is completed, the resulting time-domain waveform is ready to time-gate and transform into the frequency domain.

A virtually identical noise-reduction process was carried out for the low-frequency TEM cell calibrations, except that the SMA barrel was placed at the input connector of the cell, instead of at the base of the cone.

6. TRANSFER FUNCTION RESULTS

Sensor #36 was the only sensor that did not have an associated metallic structural component and, therefore, provided a good indication of true sensor performance. During the measurements, it was deployed as a true ground plane sensor. It was securely mounted to the ground plane with machine screws, and an excellent conductive contact was maintained. The measured results for this sensor are depicted Figs. 15 to 17. The plot of Fig. 15 depicts the average sensor receive transfer function results (for three measurements) obtained in the TEM cell for the frequency range of 10 MHz through 100 MHz. The differentiating property of this sensor is clearly evident in the logarithmic frequency plot, where the sensor response is nearly a perfect straight line with a slope very close to 20 dB/decade. The receive transfer function results are extended with measurements on the cone and ground plane system to cover the frequency range of 100 MHz to 6 GHz. The average of eight measurements is shown in Fig. 16, where the differentiating property rapidly breaks down above 100 MHz, and the sensor begins to operate as an antenna. The combined results in the overlapping frequency range of the two calibration systems are shown in Fig. 17 where the results agree well within the estimated measurement (see the last section of this report) uncertainties of the two measurement systems. A systematic offset is apparent between the two sets of measured results. The reason for this offset is not known at this time, but one strong possibility might be attributed to local field distortion effects inside the TEM cell, caused by the presence of the sensor. One aspect of the data that suggests this is the frequency-dependent variation in slope that are present on the TEM cell results, a feature not present on the cone and ground plane results. Measurements in TEM cells of various sizes and numerical

modeling of the cell/sensor combination will be required to resolve this issue in a quantitative fashion.

The measurement results for sensor #37 are summarized in Figs. 18 through 20, where characteristics very similar to those of #36 have been obtained. The results are averaged over a sequence of repeated measurements: three for the TEM cell results; 8 for the cone and ground plane. The low-frequency TEM cell results, depicted in Fig. 18, are very close to those obtained for sensor #36, with a slope that is also very close to 20 dB/decade. The cone and ground plane data of Fig. 19 track those of sensor #36 up to a frequency 3 GHz, beyond which there are noticeable differences. These differences are probably due to the discontinuity at the junction of the metal sheet and the ground plane. The overlap data, depicted in Fig. 20, exhibit similar characteristics to those previously obtained for sensor #36; and a similar offset is observed between the two measurement systems.

Although the low-frequency data of Fig. 21, obtained for sensor #33, closely track those previously obtained, dramatic differences occur with the higher frequency results of Figs. 22 and 23. A study of these two figures shows the major effects due to the presence of the metal post attached to the base plate. As expected, the loading effect of the post is most dramatic when the post is located between the sensor and the incident wave front. This is due to the shadowing effect of the post which becomes more pronounced at the higher frequencies. Although the effects of locating the post behind the probe are not as pronounced, significant effects are still noted. The lower frequency ripple in the data (in the 2 to 4 GHz range) of Fig. 23 strongly suggests an interaction of the direct wave, generated by the cone, and reflections from the post. Improved agreement is obtained between the two systems in the overlapping frequency range of Fig. 24. The improvement might very well be due to serendipitous low-frequency tuning effects caused by the post.

Both the high and low-frequency results for sensor #34 in Figs. 25 through 28 show pronounced shifts from those of sensor #36. This is primarily due to the loading effects of the elevated (approximately 0.1m) base plate on which the sensor is attached. This effect manifests itself in the upward shift (approx. 2 dB) of the low-frequency receive transfer function characteristics of Fig. 25 and in the pronounced differences between the 100 MHz to 6 GHz results of Figs. 26 and 27 for two different base plate orientations. One dramatic effect is present in Fig. 26, where a deep resonance is visible at 3.6 GHz. As can be seen by comparing Figs. 26 and 27, this resonance is strongly a function of the base plate orientation. Since the base plate is basically a rectangular waveguide transmission line section with two open ends, it forms a resonant structure that can easily be coupled to by external fields. The 3.6 GHz null is probably due to a waveguide resonance in the base plate structure. The overlap region between the TEM cell and cone and ground plane systems is shown in Fig. 28, where the agreement is excellent. It appears that the base plate provides a tuning effect in the TEM cell similar to the post of sensor # 33, resulting in better agreement than occurred for sensor #36.

The final set of results are depicted for sensor #35 in Figs. 29 and 30. The ungated time-domain waveform for this sensor is shown in Fig. 29, where it is apparent that the sensor response does not decay out before the environmental reflections occur. The longer response is due to structural resonance effects of the large aluminum box on which the sensor is mounted. Because of the sensor response does not ring down before the first major environmental reflections, this sensor cannot be calibrated with a reliable statement of uncertainty. However, receive transfer function

results are shown in Fig. 30 in which the maximum time gate has been employed (up to the point at which environmental reflections occur in the time-domain waveform). The low-frequency behavior of the sensor is totally “washed out” by the presence of the box. In fact, there is no longer a low-frequency differentiation property for this sensor.

7. UNCERTAINTIES IN THE MEASUREMENT SYSTEMS

There are two main contributing factors to the measurement uncertainty:

1. Uncertainties introduced by the field generation system and the associated instrumentation and cables.
2. Uncertainties introduced by the placement of the sensor in the generated standard field.

The measurement uncertainties introduced by both the TEM cell and cone and ground plane standard-field generation systems have been carefully analyzed by Ondrejka and Johnk in a NIST technical note that is currently in preparation [9]. These standard-field generation systems are analyzed in this technical note using a Type B uncertainty analysis that uses analytical formulas in conjunction with assumed uniform a priori probability distributions [10]. The results of this analysis are summarized in Tables 1 and 2 below.

Table 1. Type B expanded uncertainties (from Ref. [9]) for sensor calibrations in the NIST 1.2m TEM cell field generation system with an assumed confidence level of 95%.

Source of error	Nominal value of system parameter	Relative measurement uncertainty
Ceptum distance, D	0.55 m	$\pm 0.2\%$
Generated field uniformity	$\pm 20\%$	$\pm 2.3\%$
Sensor aperture integration effects	$\pm 10\%$	$\pm 4.0\%$
Measured voltage ratio	(variable)	$\pm 0.2\%$
Reference attenuator	0.001 (30 dB)	$\pm 0.6\%$
Cable mismatches	1.0 ± 0.04	$\pm 0.07\%$
Sensor impedance effects	$ \Gamma = \pm 1$; $r = \pm 0.02$ m	$\pm 5.7\%$
Total relative uncertainty in $ TF_R $	(variable)	$\pm 7.7\%$

Table 2. Type B expanded uncertainties (from Ref. [9]) for sensor calibrations in the NIST 1.2 m cone and ground plane cell field generation system with an assumed confidence level of 95%.

Nominal value of system parameter	Source of error	Relative Measurement Uncertainty
(variable)	Distance from cone base to sensor	$\pm 0.1\%$
90°	Sensor position angle θ (see eq 2)	$\pm 0.05\%$
4°	Cone angle θ_0	$\pm 0.4\%$
(variable)	Measured voltage ratio	$\pm 0.2\%$
0.001 (30 dB)	Reference attenuator	$\pm 0.6\%$
1.0 ± 0.04	Cable mismatches	$\pm 0.1\%$
$ \Gamma = \pm 1$; $r = \pm 0.02$ m	Sensor impedance effects	$\pm 9.9\%$
(variable)	Total relative uncertainty in $ TF_R $	$\pm 10.1\%$

While the uncertainties listed in the tables provide a complete description of the components of errors in the two systems in terms of intrinsic field generation capabilities they do not completely account for effects introduced by the sensor under test. One significant source of sensor effects that are not accounted for in the Type B analysis is due to the sensor support structures (see Fig. 2). Since the support structure is exposed to the illuminating field, it becomes part of the sensor itself and affects the receive transfer function. These effects are caused by structural resonances, contact with the ground plane (or TEM cell floor), and the resulting modifications in the sensor receiving aperture plane. These effects could be accounted for using a Type B analysis, at least to some extent, using sophisticated numerical modeling of the measurement system and the sensor under test, but such an endeavor would be a formidable task indeed. Clearly, a significant effort is needed to account for the systematic effects introduced by the sensor support structures. However, such an undertaking is beyond the scope of this effort.

The random effects of the sensor mounts that are not covered in the Type B uncertainty analysis, however, can be accounted for by a Type A statistical analysis, based on repeated sensor measurements. In this effort, each sensor measurement was performed either three or eight times. In addition, at the conclusion of each measurement trial, the sensor was completely dismantled from the measurement system, and the interconnecting sensor and generator cables were

completely disconnected in order to eliminate potential statistical bias. In order to assess system stability and reproducibility, the system was shut down for a minimum of 24 hours after several trials were completed. The sequence of measurements was then completed at later date after a suitable warm-up time for the equipment. The results of the Type A analysis are summarized in Table 3.

Table 3. Type A relative uncertainties computed from the student's t-distribution [10,11] for a 95% level of confidence.

Measurement system	Freq. MHz	Sensor 36 type A relative uncertainty (n= # of meas.)	Sensor 37 type A relative uncertainty (n= # of meas.)	Sensor 33 type A relative uncertainty (n= # of meas.)	Sensor 34 type A relative uncertainty (n= # of meas.)	Sensor 34R type A relative uncertainty (n= # of meas.)
TEM Cell	25	$\pm 4.0\%$ (n = 3)	$\pm 4.6\%$ (n = 3)	$\pm 4.0\%$ (n = 3)	$\pm 1.6\%$ (n = 3)	-----
Cone and Ground Plane	173	$\pm 1.7\%$ (n = 8)	$\pm 1.4\%$ (n = 8)	$\pm 1.8\%$ (n = 8)	$\pm 0.9\%$ (n = 8)	$\pm 1.4\%$ (n = 3)
Cone and Ground Plane	430	$\pm 1.9\%$ (n = 8)	$\pm 2.3\%$ (n = 8)	$\pm 4.5\%$ (n = 8)	$\pm 1.9\%$ (n = 8)	$\pm 3.9\%$ (n = 3)
Cone and Ground Plane	2700	$\pm 2.4\%$ (n = 8)	$\pm 2.4\%$ (n = 8)	$\pm 7.3\%$ (n = 8)	$\pm 1.6\%$ (n = 8)	$\pm 0.5\%$ (n = 3)
Cone and Ground Plane	5400	$\pm 7.9\%$ (n = 8)	$\pm 15.2\%$ (n = 8)	$\pm 4.0\%$ (n = 8)	$\pm 7.8\%$ (n = 8)	$\pm 3.7\%$ (n = 8)

Because of the small number of trials involved, the correct distribution for the evaluation of the uncertainties is the student's t-distribution given in refs. [10,11,12]. This distribution is used for statistical evaluations when the number of repeated experiments is less than 30 [11,12]. The student's t-distribution rigorously accounts for the higher uncertainties that result from conducting fewer measurement trials. As an inspection of Table 3 reveals, it is interesting to note that in some instances, the measurement uncertainties increase dramatically with frequency. This occurs, for example, for sensor #37 where the combined measurement uncertainty increases fivefold from 2700 to 5400 MHz. The data obtained indicated that this increase in uncertainty was primarily due to the contact variations between the sensor support structure and the ground plane.

The overall measurement uncertainties can now be found by combining the Type A and Type B uncertainties in quadrature [12], by taking the square root of the sum of squares of the uncertainty components. The combined measurement uncertainties, along with the nominal receive transfer function are tabulated in Table 4 below.

Table 4. NASA D-dot sensor average receive transfer function results, along with associated combined standard uncertainties (95% level of confidence). Note: bp denotes the support structure of sensor #34.

Frequency MHz	Sensor #36 $ TF_R $ dB	Sensor #37 $ TF_R $ dB	Sensor #33 $ TF_R $ dB post behind sensor	Sensor #34 $ TF_R $ dB narrow bp dim to incident wavefront	Sensor #34R $ TF_R $ dB bp rotated 90°
25	-43.5 ± 0.7	-43.0 ± 0.8	-42.8 ± 0.7	-50.0 ± 0.7	-----
173	-25.9 ± 0.9	-25.6 ± 0.9	-25.4 ± 0.9	-25.4 ± 0.9	-21.9 ± 0.9
430	-24.5 ± 0.9	-24.0 ± 0.9	-23.5 ± 0.9	-21.2 ± 0.9	-26.4 ± 0.9
2700	-40.5 ± 0.9	-40.5 ± 0.9	-41.3 ± 1.0	-42.3 ± 0.9	-40.9 ± 0.9
5400	-46.5 ± 1.0	-46.1 ± 0.9	-50.9 ± 0.9	-50.6 ± 1.0	-45.8 ± 1.1

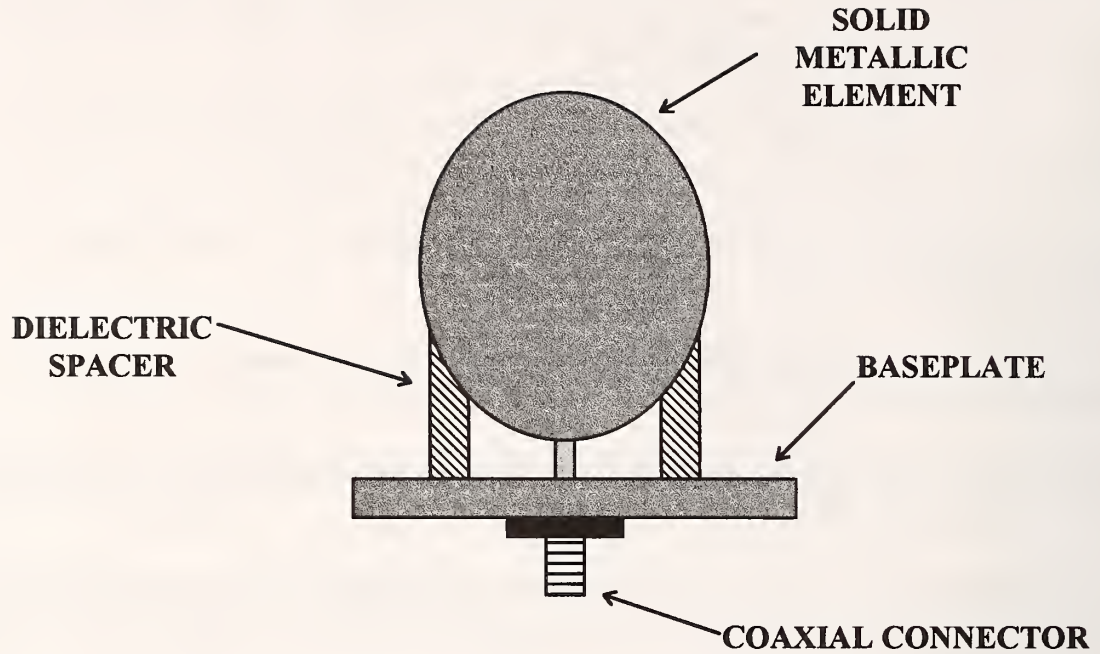
8. CONCLUSIONS

The results of the measurements demonstrate the power and simplicity of direct-pulse time-domain methods in performing broadband sensor calibrations. The sensor data obtained using the NIST 1.2 m TEM cell and the cone and ground plane standard-field generation system covered a frequency band spanning nearly three decades. Accurate broadband response data were obtained on the five sensors for use in NASA electromagnetic compatibility studies, and they enabled NASA to obtain vital electromagnetic field intensity data for a large commercial aircraft flown close to high-power electromagnetic radiators.

9. REFERENCES

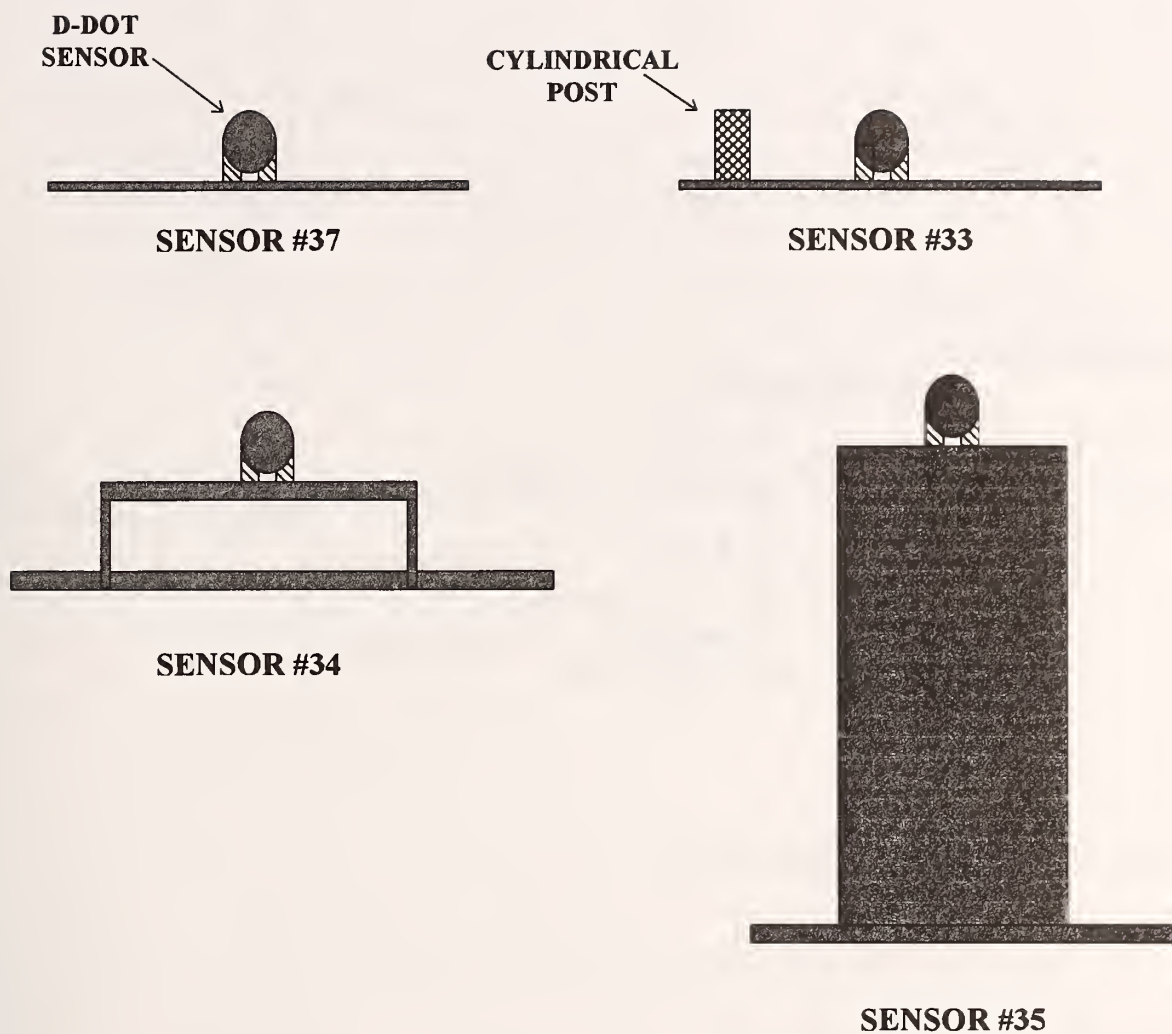
- [1] C. E. Baum, E.L. Breen, J. C. Giles, J. O'Neill, and G. D. Sower, "Sensors for electromagnetic pulse measurements both inside and away from nuclear source regions," IEEE Trans. Electromag. Compat., vol. 20, no. 1, Feb. 1978.
- [2] M. Kanda and R. D. Orr, "Generation of Standard Electromagnetic Fields in a TEM Cell," Nat. Bur. Stand. (U.S.) Tech. Note 1319, Aug. 1988.

- [3] R. A. Lawton and A. Ondrejka, "Antennas and the associated time-domain range for the measurement of impulsive fields," Nat. Bur. Stand. (U.S.) Tech. Note 1008, Nov. 1978.
- [4] A. Ondrejka, J. Ladbury, and H. Medley, "TEM Horn Antenna Design Guide," Natl. Inst. Stand. Technol. Tech Note, to be published.
- [5] J. R. Andrews, M. G. Arthur, "Spectrum Amplitude—Definition, Generation and Measurement," Nat. Bur. Stand. (U.S.) Tech. Note 699, Oct. 1977.
- [6] A. V. Oppenheim and R. W. Schaffer, *Digital Signal Processing*, Prentice-Hall, Inc., Englewood Cliffs, N. J., 1975.
- [7] N. S. Nahman and M. E. Guillaume, "Deconvolution of time-domain waveforms in the presence of noise," Nat. Bur. Stand. Tech Note (U.S.) 1047, Oct. 1981.
- [8] R. T. Johnk, "Two-dimensional electrostatic TEM cell field mapping code," Unpublished Fortran Code, (developed at NIST Oct. 1992).
- [9] A. Ondrejka and R. T. Johnk, "Sensor and antenna calibration methods using NIST standard field generation techniques and the three antenna method," Natl. Inst. Stand. Technol. Tech. Note, in preparation.
- [10] B. N. Taylor and C. E. Kuyatt, "Guidelines for evaluating and expressing the uncertainty of NIST measurement results, Natl. Inst. Stand. Technol. Tech. Note 1297, Sept. 1994.
- [11] G. W. Snedecor and W. G. Cochran, *Statistical Methods*, Iowa State University Press, Ames, Iowa, 1972.
- [12] J. R. Taylor, *An Introduction to Error Analysis*, University Science Books, Sausalito, CA, 1982.



D-DOT SENSOR (SIDE VIEW)

Figure 1. Basic features of the D-Dot sensor used in the NASA evaluation effort.



SENSOR MOUNTS (SIDE VIEW)

Figure 2. Support structures for sensors #33, #34, #35, and #37. Sensor #36 had no supporting structure other than the small base plate shown in Figure 1.

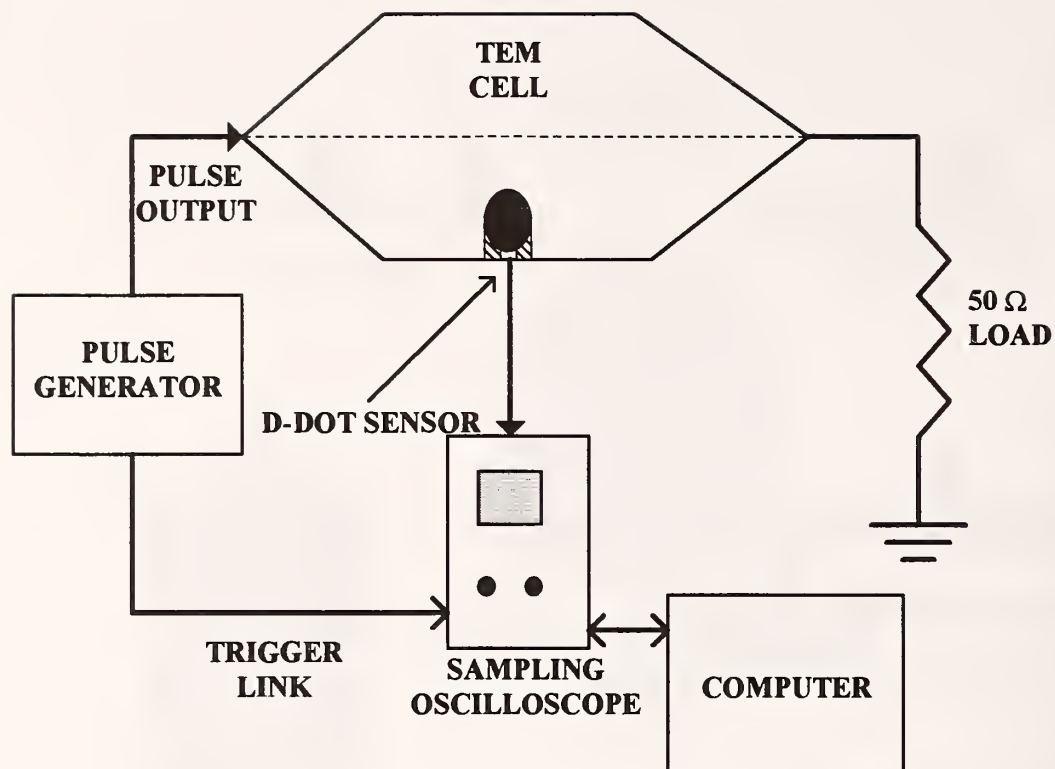


Figure 3. TEM cell sensor calibration setup.

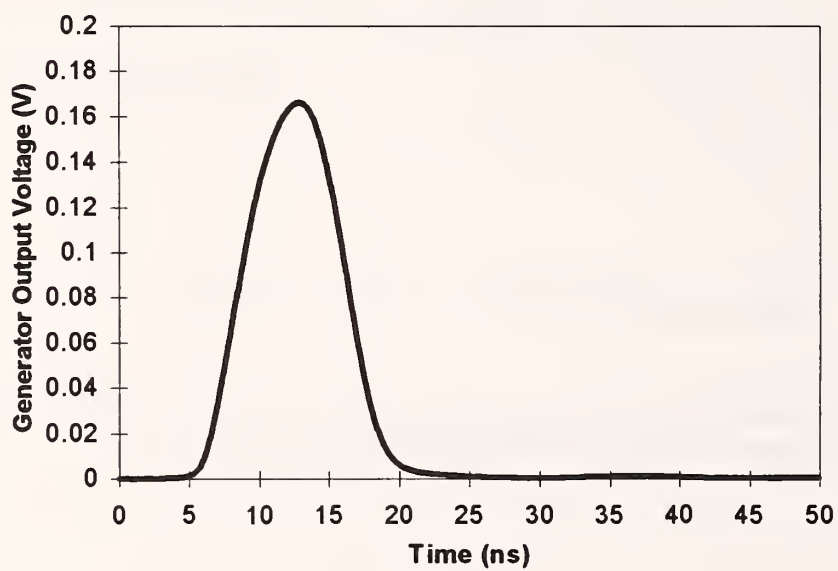


Figure 4. Low-frequency pulse generator output used for the TEM cell sensor calibrations.

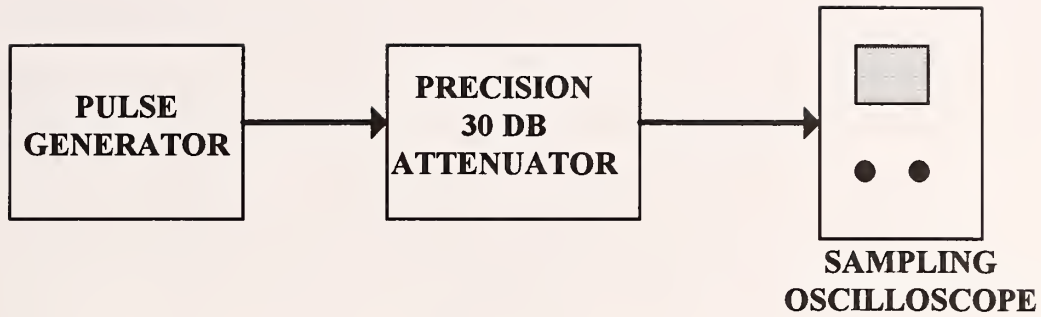


Figure 5. Reference waveform acquisition setup for both TEM cell and cone and ground plane sensor calibrations.

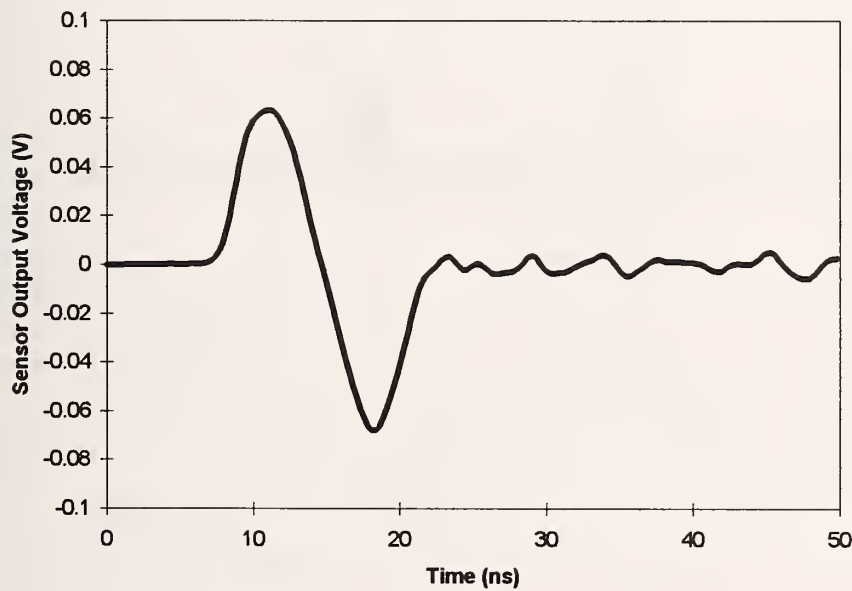


Figure 6. Sensor #36 output waveform obtained with the TEM cell standard field generation system using the generator waveform of Fig. 4.

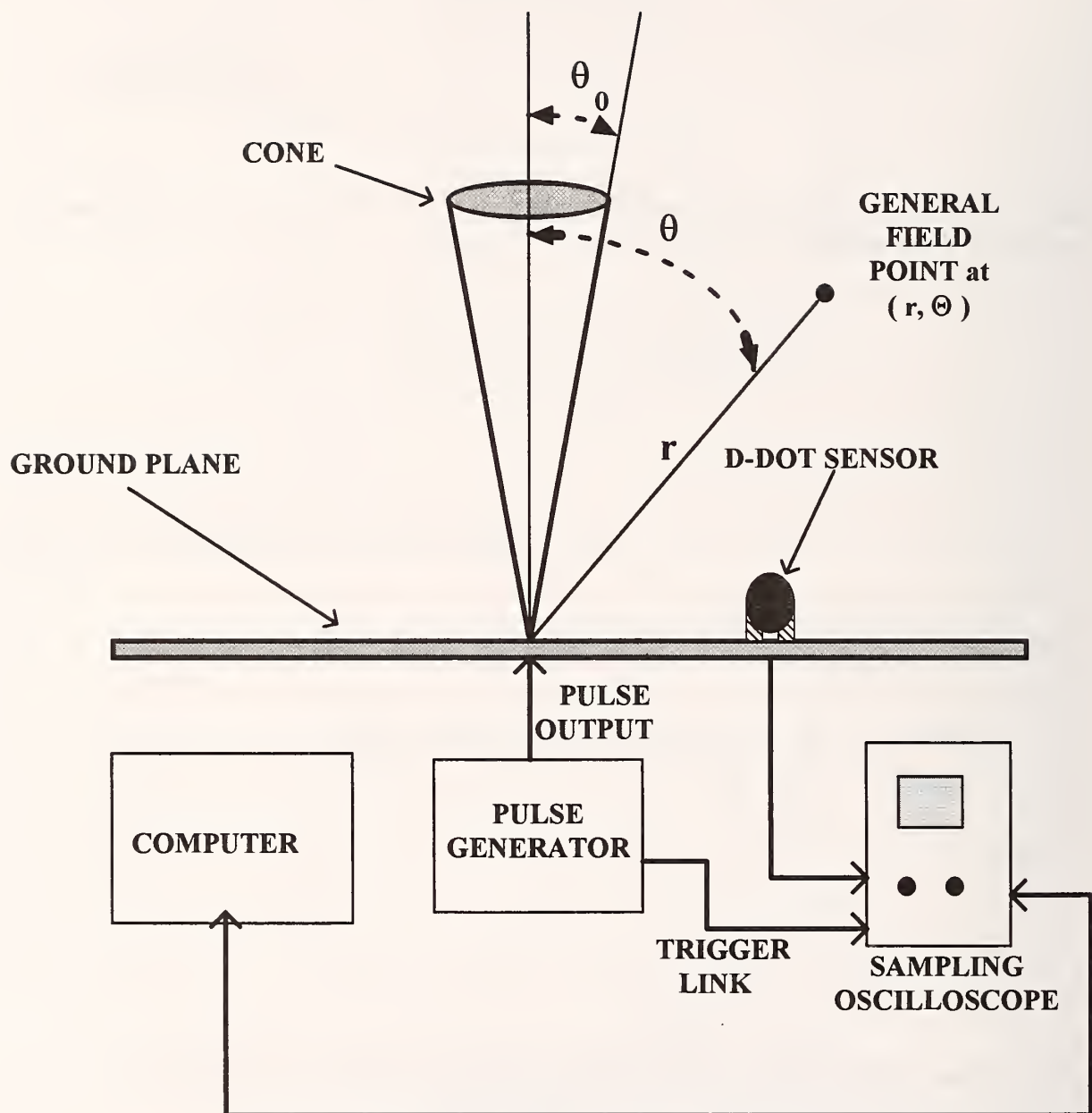


Figure 7. Cone and ground plane sensor calibration setup.

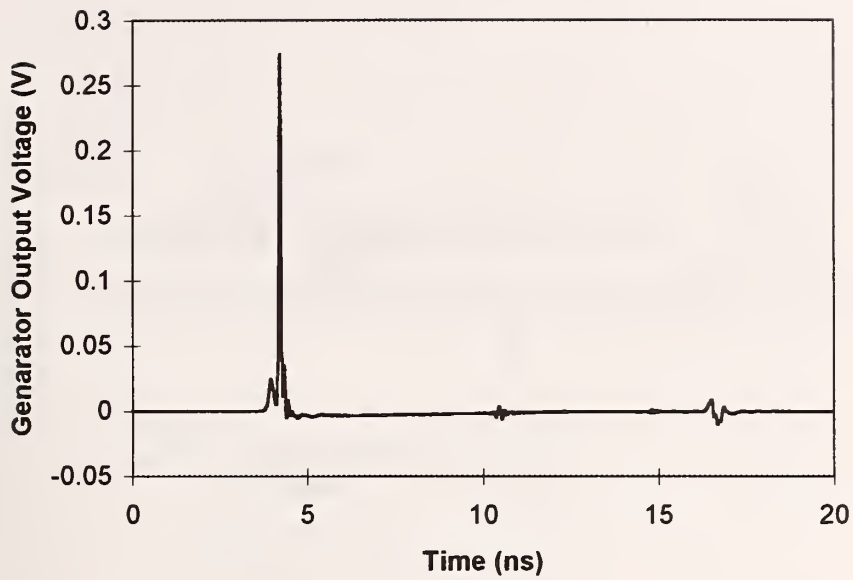


Figure 8. High-frequency pulse generator output used for the cone and ground plane sensor calibrations.

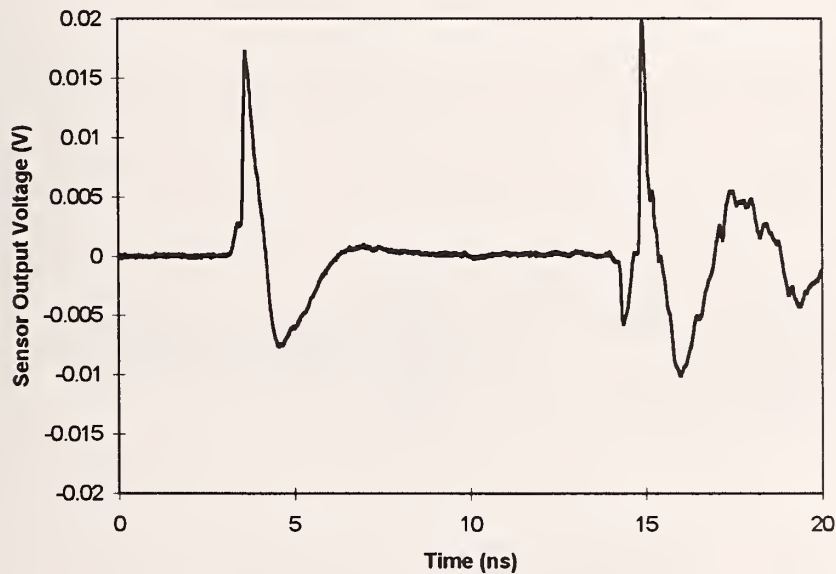


Figure 9. Sensor #36 output waveform obtained with the cone and ground plane standard field generation system using the generator waveform of Figure 8.

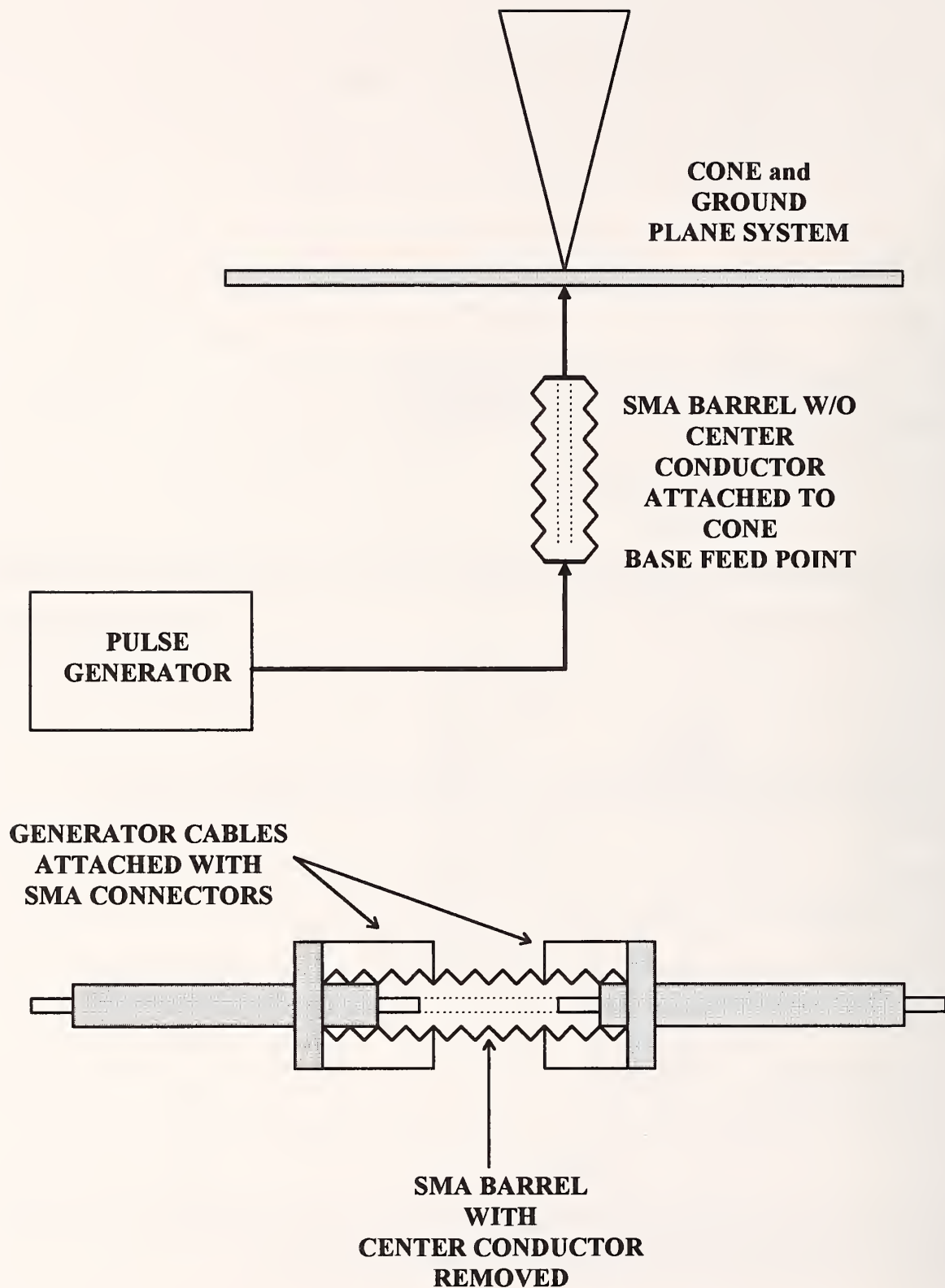


Figure 10. Pre-trigger common-mode signal removal using SMA coaxial barrel without a center conductor.

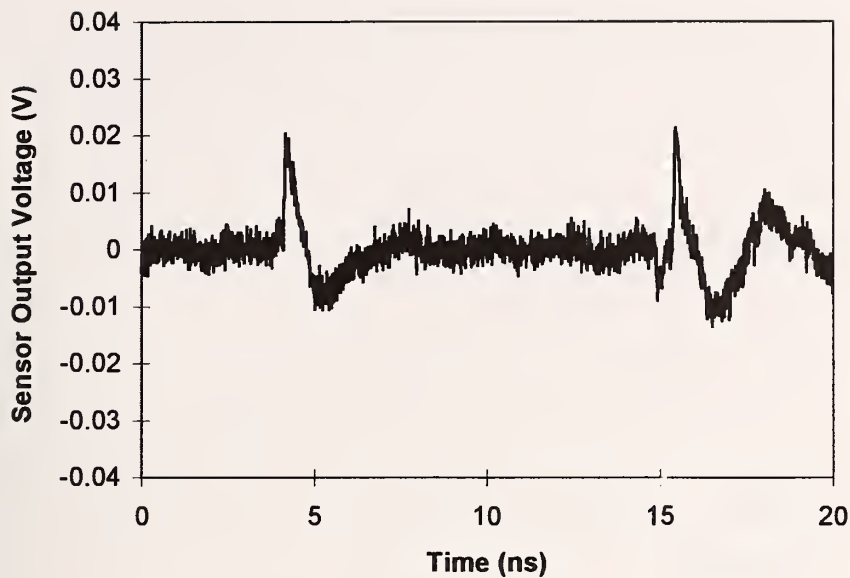


Figure 11. Raw sensor #37 output obtained with the cone and ground plane system without averaging or common-mode signal removal.

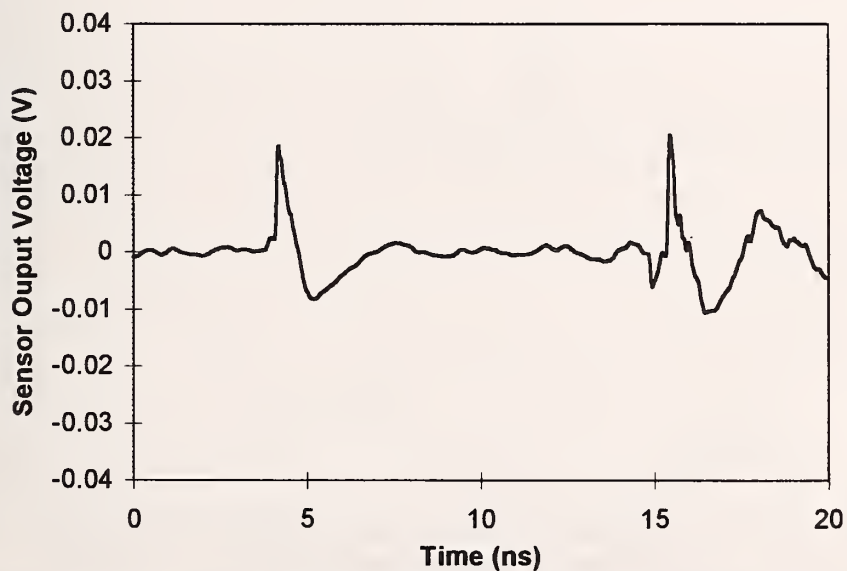


Figure 12. Raw sensor #37 output obtained with the cone and ground plane system with 1024 averages. Note the significant reduction in high-frequency random variations.

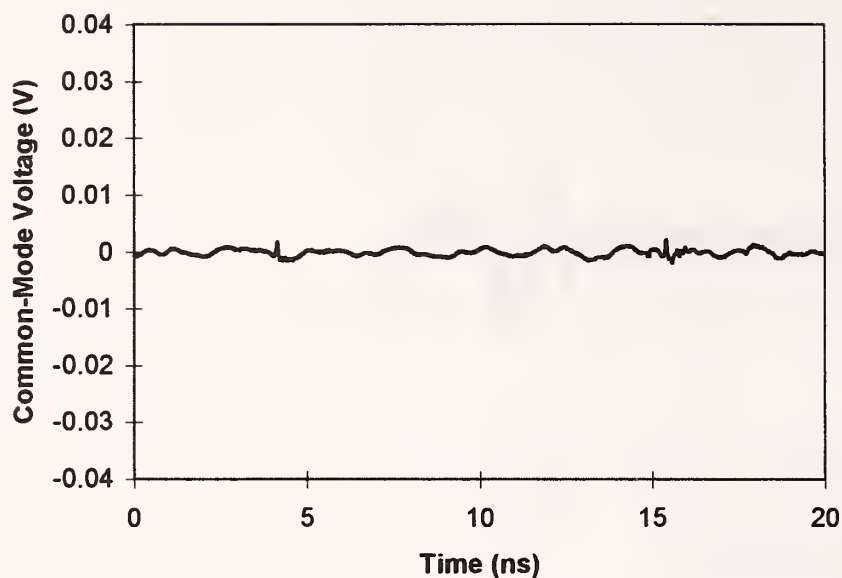


Figure 13. Pre-trigger common mode signal detected by sensor #37. 1024 averages.

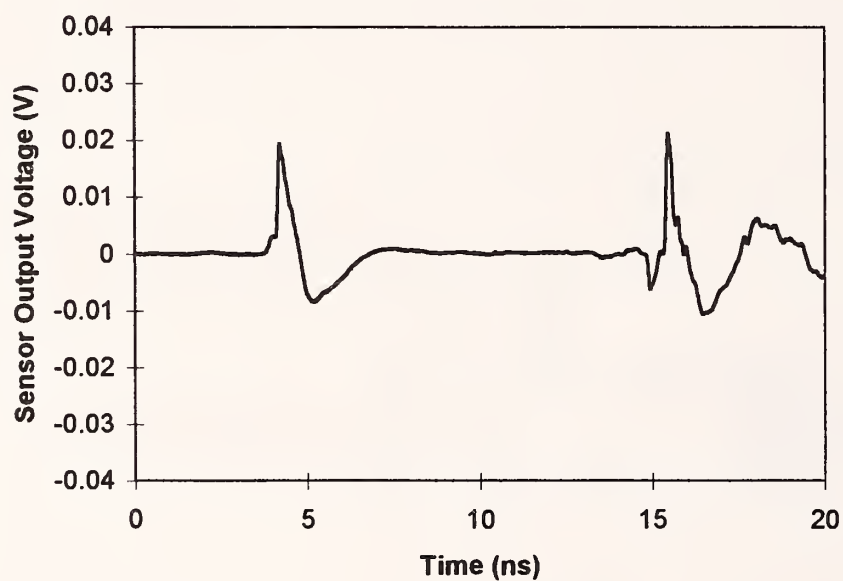


Figure 14. Sensor #37 output after 1024 averages and pre-trigger common-mode signal removal. The sensor response occurs approximately in the range of 3 ns to 9 ns, and the environmental reflections begin at approximately at 11 ns.

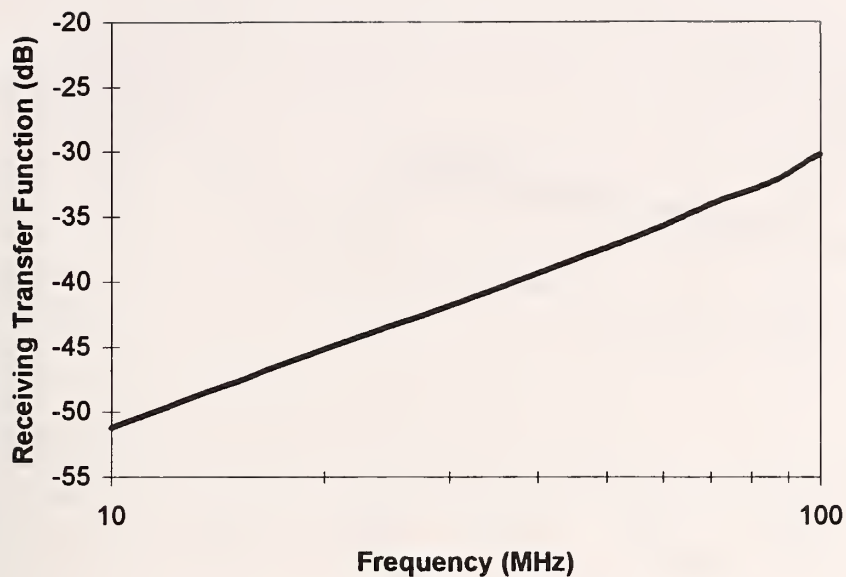


Figure 15. Sensor #36 receiving transfer function results obtained with the TEM cell standard field generation system.

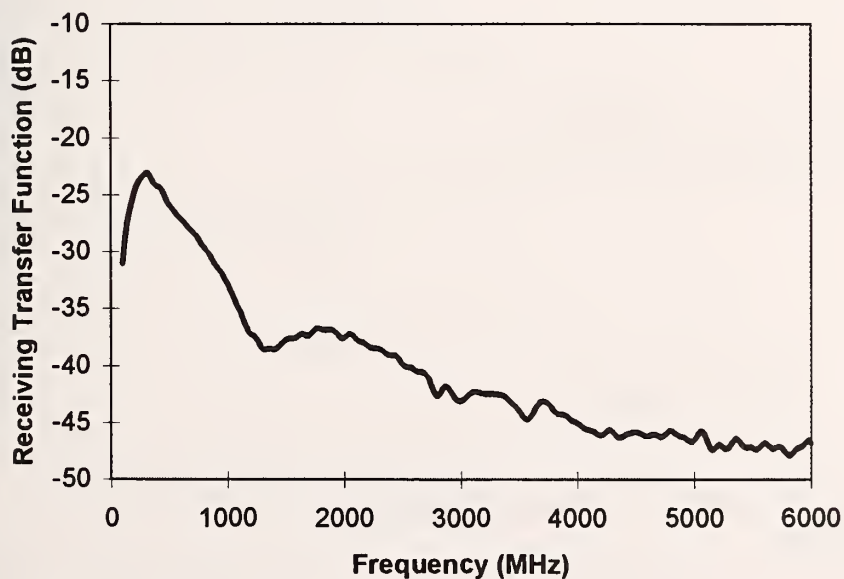


Figure 16. Sensor #36 receiving transfer function results obtained with the cone and ground plane standard field generation system.

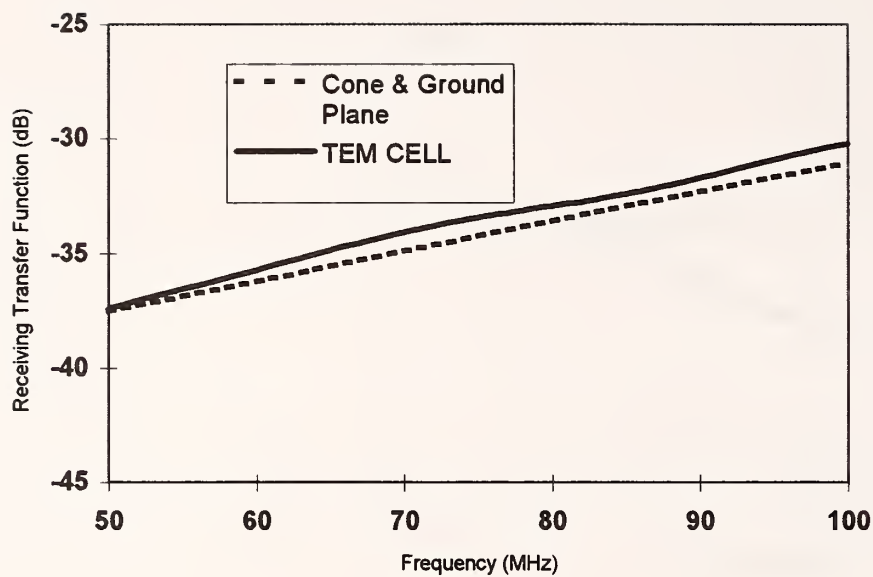


Figure 17. Intercomparison of sensor #36 receiving transfer function results obtained with the TEM cell and cone and ground plane standard-field generation systems.

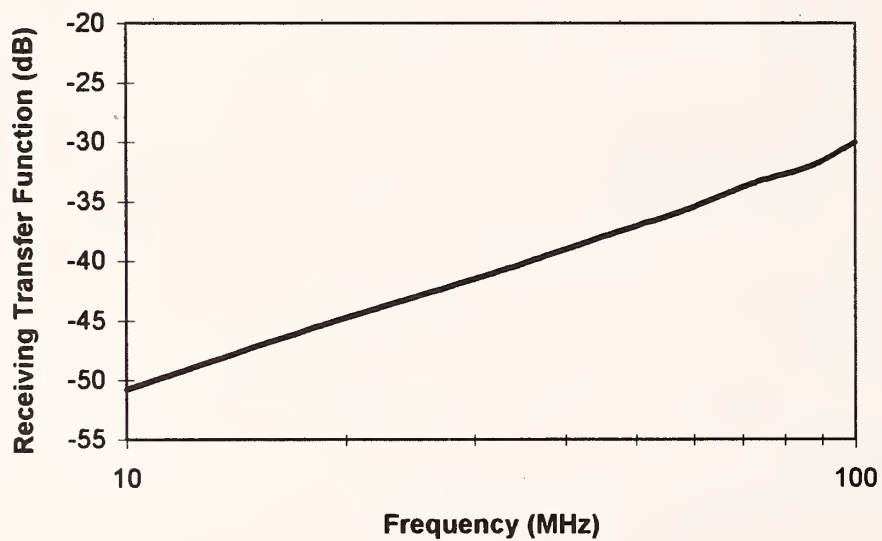


Figure 18. Sensor #37 receiving transfer function results obtained with the TEM cell standard field generation system.

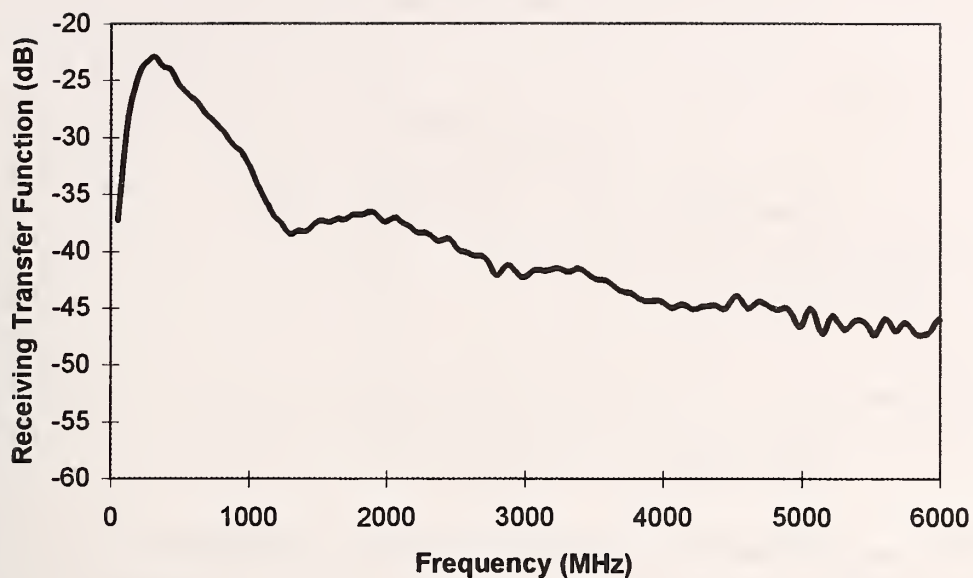


Figure 19. Sensor #37 receiving transfer function results obtained with the cone and ground plane standard field generation system.

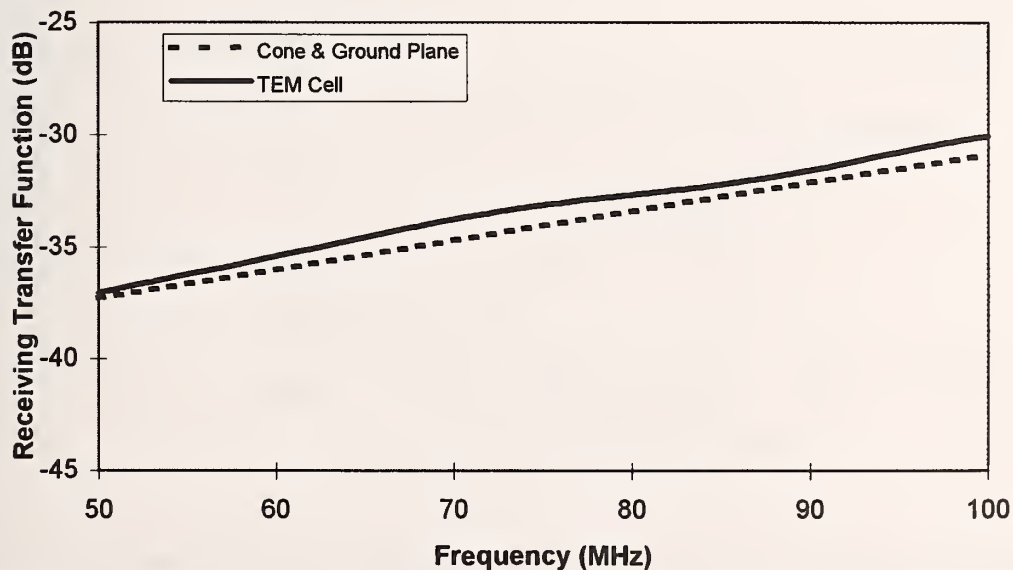


Figure 20. Intercomparison of sensor #37 receiving transfer function results obtained with the TEM cell and cone and ground plane standard-field generation systems.

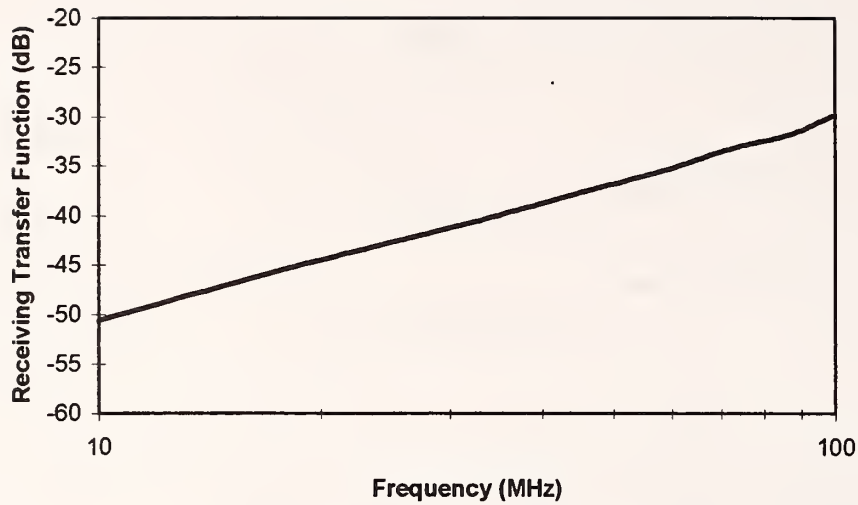


Figure 21. Sensor #33 receiving transfer function results obtained with the TEM cell standard field generation system. These data were obtained with the cylindrical post behind the sensor (with respect to the incident wavefront).

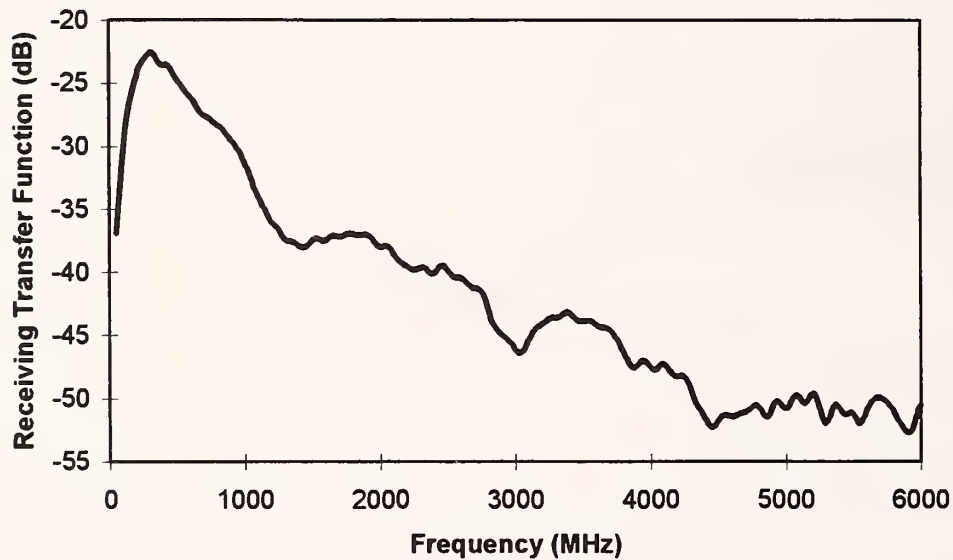


Figure 22. Sensor #33 receiving transfer function results obtained with the cone and ground plane standard field generation system. These data were obtained with the cylindrical post behind the sensor (with respect to the incident wavefront).

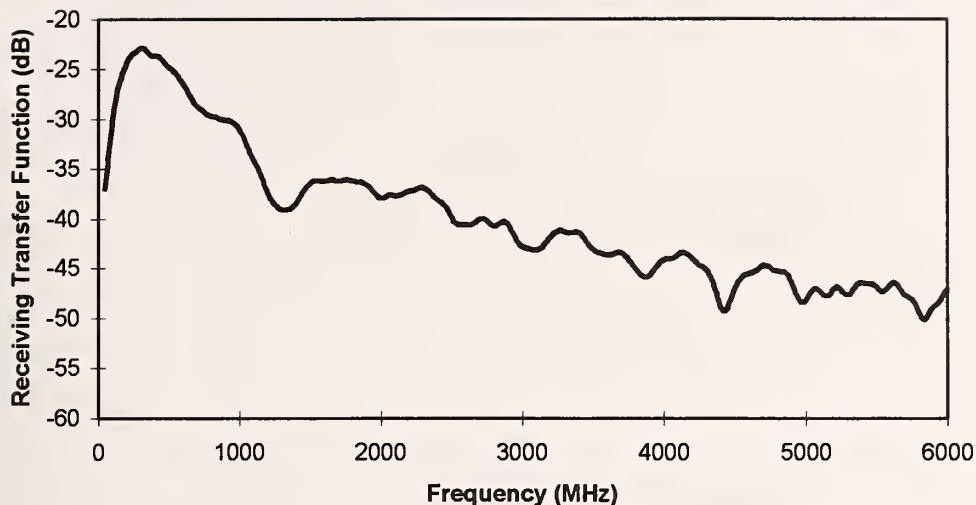


Figure 23. Sensor #33 receiving transfer function results obtained with the cone and ground plane standard field generation system. These data were obtained with the cylindrical post in front of the sensor (with respect to the incident wavefront).

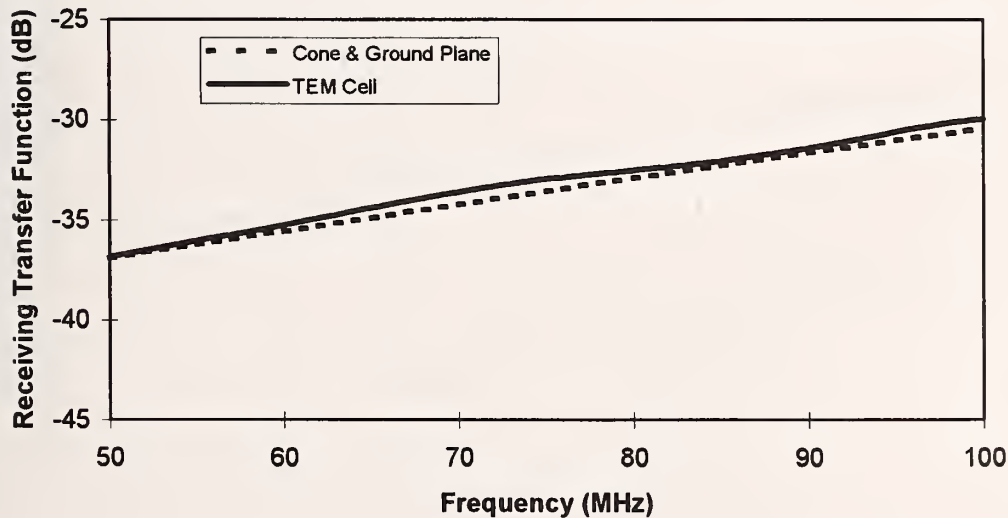


Figure 24. Intercomparison of sensor #33 receive transfer function results obtained with the TEM cell and cone and ground plane standard-field generation systems. These data were obtained with the cylindrical post behind the sensor (with respect to the incident wavefront).

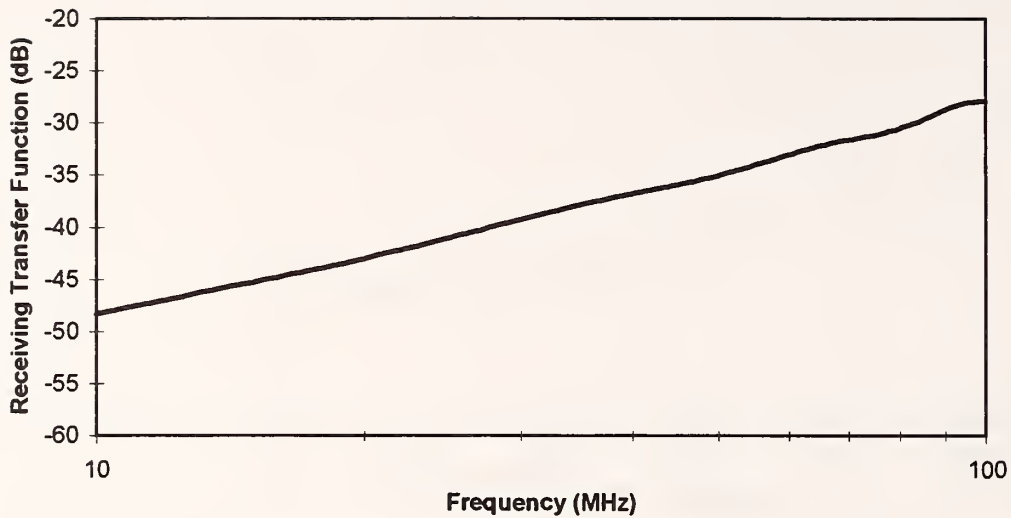


Figure 25. Sensor #34 receiving transfer function results obtained with the TEM cell standard field generation system. These data were obtained with the narrow baseplate dimension parallel to the incident wavefront.

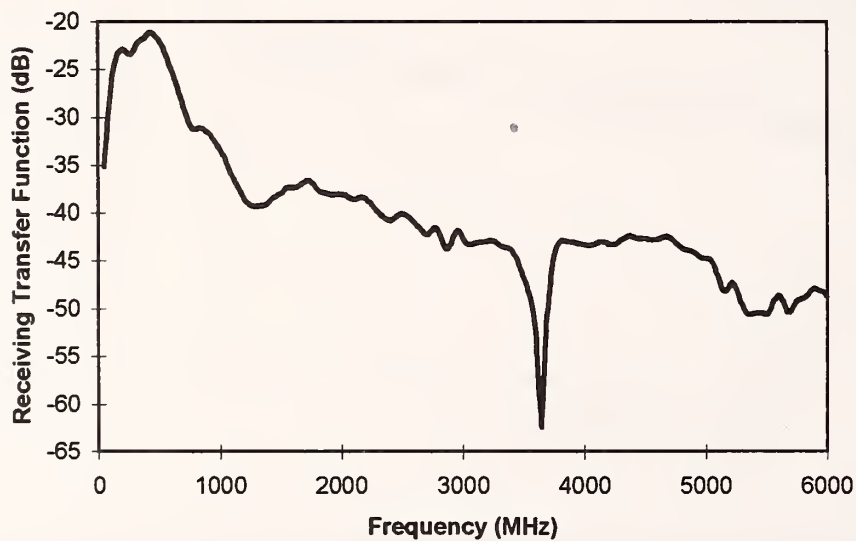


Figure 26. Sensor #34 receiving transfer function results obtained with the cone and ground plane standard field generation system. These data were obtained with the narrow baseplate dimension parallel to the incident wavefront.

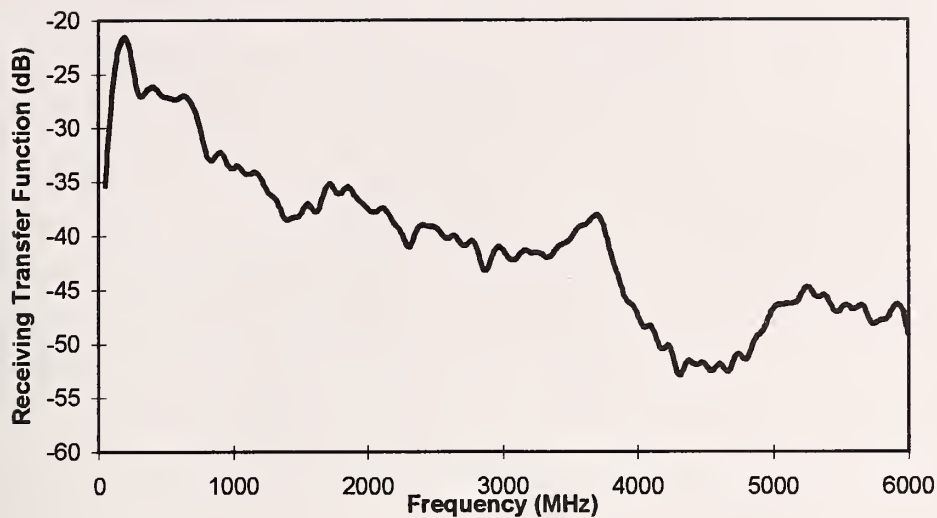


Figure 27. Sensor #34 receiving transfer function results obtained with the cone and ground plane standard field generation system. These data were obtained with the wide baseplate dimension parallel to the incident wavefront.

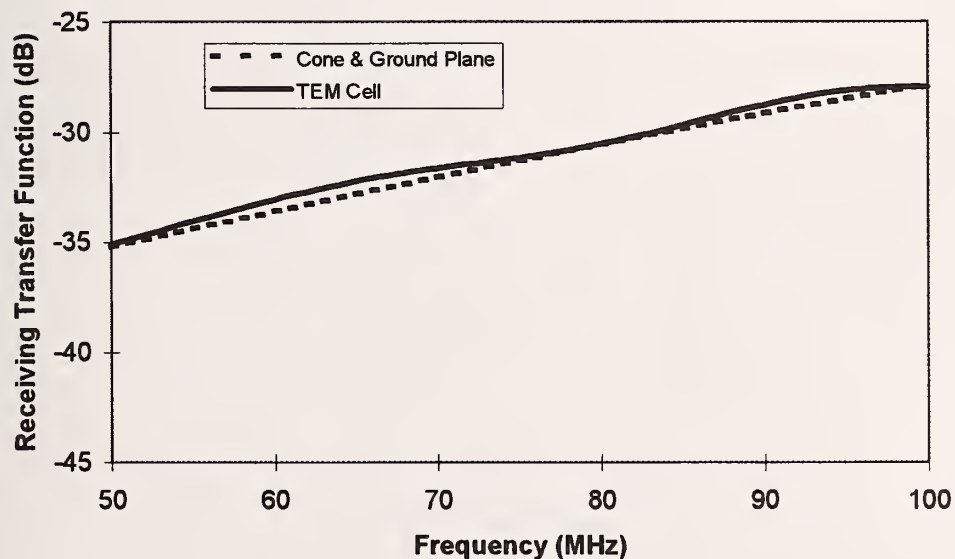


Figure 28. Intercomparison of sensor #34 receiving transfer function results obtained with the TEM cell and cone and ground plane standard-field generation systems. These data were obtained with the narrow baseplate dimension parallel to the incident wavefront.

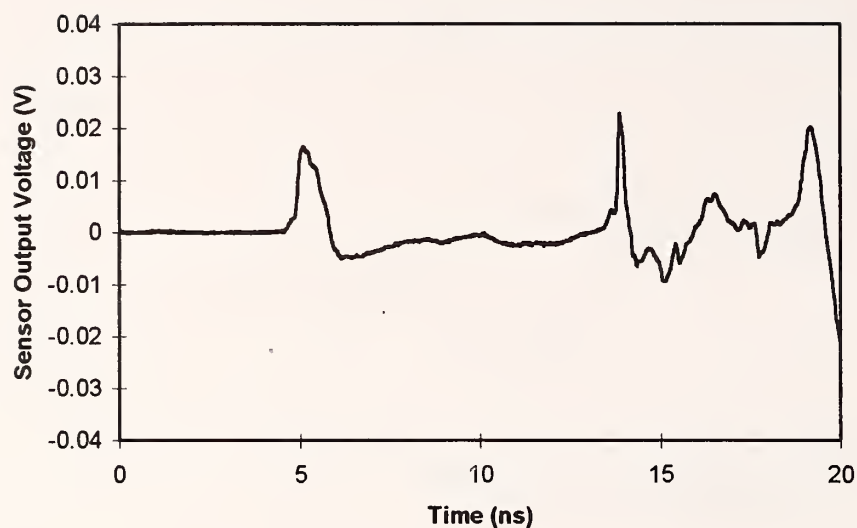


Figure 29. Ungated sensor #35 time-domain response obtained on the cone and ground plane standard-field generation system. Note that the sensor response is extended by resonances in the support structure.

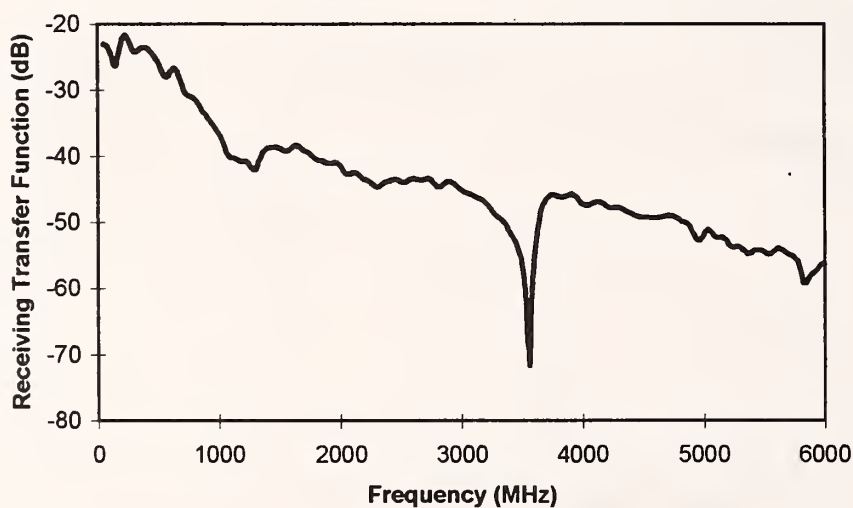


Figure 30. Sensor #35 receiving transfer function results obtained with the cone and ground plane standard field generation system.

NIST Technical Publications

Periodical

Journal of Research of the National Institute of Standards and Technology—Reports NIST research and development in those disciplines of the physical and engineering sciences in which the Institute is active. These include physics, chemistry, engineering, mathematics, and computer sciences. Papers cover a broad range of subjects, with major emphasis on measurement methodology and the basic technology underlying standardization. Also included from time to time are survey articles on topics closely related to the Institute's technical and scientific programs. Issued six times a year.

Nonperiodicals

Monographs—Major contributions to the technical literature on various subjects related to the Institute's scientific and technical activities.

Handbooks—Recommended codes of engineering and industrial practice (including safety codes) developed in cooperation with interested industries, professional organizations, and regulatory bodies.

Special Publications—Include proceedings of conferences sponsored by NIST, NIST annual reports, and other special publications appropriate to this grouping such as wall charts, pocket cards, and bibliographies.

Applied Mathematics Series—Mathematical tables, manuals, and studies of special interest to physicists, engineers, chemists, biologists, mathematicians, computer programmers, and others engaged in scientific and technical work.

National Standard Reference Data Series—Provides quantitative data on the physical and chemical properties of materials, compiled from the world's literature and critically evaluated. Developed under a worldwide program coordinated by NIST under the authority of the National Standard Data Act (Public Law 90-396). NOTE: The Journal of Physical and Chemical Reference Data (JPCRD) is published bi-monthly for NIST by the American Chemical Society (ACS) and the American Institute of Physics (AIP). Subscriptions, reprints, and supplements are available from ACS, 1155 Sixteenth St., NW, Washington, DC 20056.

Building Science Series—Disseminates technical information developed at the Institute on building materials, components, systems, and whole structures. The series presents research results, test methods, and performance criteria related to the structural and environmental functions and the durability and safety characteristics of building elements and systems.

Technical Notes—Studies or reports which are complete in themselves but restrictive in their treatment of a subject. Analogous to monographs but not so comprehensive in scope or definitive in treatment of the subject area. Often serve as a vehicle for final reports of work performed at NIST under the sponsorship of other government agencies.

Voluntary Product Standards—Developed under procedures published by the Department of Commerce in Part 10, Title 15, of the Code of Federal Regulations. The standards establish nationally recognized requirements for products, and provide all concerned interests with a basis for common understanding of the characteristics of the products. NIST administers this program in support of the efforts of private-sector standardizing organizations.

Consumer Information Series—Practical information, based on NIST research and experience, covering areas of interest to the consumer. Easily understandable language and illustrations provide useful background knowledge for shopping in today's technological marketplace.

Order the above NIST publications from: Superintendent of Documents, Government Printing Office, Washington, DC 20402.

Order the following NIST publications—FIPS and NISTIRs—from the National Technical Information Service, Springfield, VA 22161.

Federal Information Processing Standards Publications (FIPS PUB)—Publications in this series collectively constitute the Federal Information Processing Standards Register. The Register serves as the official source of information in the Federal Government regarding standards issued by NIST pursuant to the Federal Property and Administrative Services Act of 1949 as amended, Public Law 89-306 (79 Stat. 1127), and as implemented by Executive Order 11717 (38 FR 12315, dated May 11, 1973) and Part 6 of Title 15 CFR (Code of Federal Regulations).

NIST Interagency Reports (NISTIR)—A special series of interim or final reports on work performed by NIST for outside sponsors (both government and non-government). In general, initial distribution is handled by the sponsor; public distribution is by the National Technical Information Service, Springfield, VA 22161, in paper copy or microfiche form.

U.S. Department of Commerce
National Institute of Standards and Technology
325 Broadway
Boulder, Colorado 80303-3328

Official Business
Penalty for Private Use, \$300